# Epitaxial Growth of ZSM-5@Silicalite-1: A Core—Shell Zeolite Designed with Passivated Surface Acidity

Arian Ghorbanpour,[†] Abhishek Gumidyala,[‡] Lars C. Grabow,[†] Steven P. Crossley,[‡] and Jeffrey D. Rimer*,[†]

[†]Department of Chemical and Biomolecular Engineering, University of Houston, 4800 Calhoun Road, Houston, Texas 77204, United States and [‡]Department of Chemical, Biological, and Materials Engineering, University of Oklahoma, 100 East Boyd Street, Norman, Oklahoma 73019, United States

ABSTRACT The design of materials with spatially controlled chemical composition has potential advantages for wide-reaching applications that span energy to medicine. Here, we present a method for preparing a core—shell aluminosilicate zeolite with continuous translational symmetry of nanopores and an epitaxial shell of tunable thickness that passivates Brønsted acid sites associated with framework Al on exterior surfaces. For this study, we selected the commercially relevant MFI framework type and prepared core—shell particles consisting of an aluminosilicate core (ZSM-5) and a siliceous shell (silicalite-1). Transmission electron microscopy and gas adsorption studies confirmed that silicalite-1 forms an epitaxial layer on ZSM-5 crystals without blocking pore openings. Scanning electron microscopy and dynamic light scattering were used in combination to confirm that the shell thickness can be tailored with nanometer resolution (e.g., 5—20 nm). X-ray photoelectron spectroscopy and temperature-programmed desorption measurements revealed the presence of a siliceous shell, while probe reactions using molecules that were either too large or adequately sized to access MFI pores confirmed the uniform shell coverage. The synthesis of ZSM-5@silicalite-1 offers a pathway for tailoring the physicochemical properties of MFI-type materials, notably in the area of catalysis, where surface passivation can enhance product selectivity without sacrificing catalyst activity. The method described herein may prove to be a general platform for zeolite core—shell design with potentially broader applicability to other porous materials.
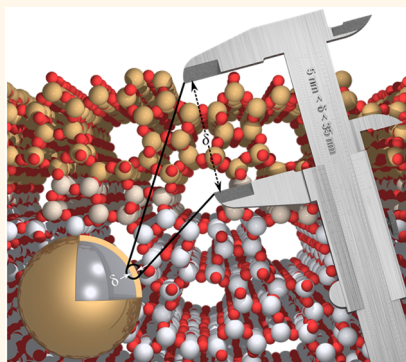
KEYWORDS: zeolite · MFI · core—shell · epitaxy · passivation · heterogeneous catalysis

Zeolites are used in a variety of applications owing to their unique acidity and nanoporous structures that are well-suited for catalysis, ion-exchange, sorption, and separations. The acidity of H-zeolites is attributed to Brønsted acid sites, which are located on oxygen atoms that bridge Si and Al atoms in the crystalline framework. In catalytic applications, Brønsted acid sites located within confined nanopores impose shape-selectivity to achieve narrow product distributions; however, acid sites on the exterior surfaces of zeolite crystals reduce product selectivity and can exhibit properties that differ from bulk sites.[1,2] A catalyst "passivation" method was patented by Mobil in the 1970s to coat ZSM-5 (MFI type) surfaces with a catalytically inactive silica layer.[3] Surface passivation has proven to be a useful method for enhancing product selectivity in the production of para-xylene[4] and para-selective disproportionation and alkylation

of aromatics.[5] The common catalyst deactivation route via external pore mouth plugging[6] could serve as justification for surface passivation as well. Additional examples include the production of methylamines using a passivated zeolite catalyst (RHO framework type) with enhanced selectivity for dimethylamine.[7]

Details regarding the synthesis and characterization of passivated zeolites are difficult to extract from patents. In addition, techniques reported in the literature tend to have associated drawbacks. Examples include postsynthesis dealumination by acid treatment, which can generate crystal defects and/or mesopores.[8—10] An alternative approach is the modification of external functional groups on zeolite surfaces with a passivating agent. Examples include the use of metal oxides (e.g., Sb_2O_3)[11] and hydride, alkyl, or alkoxy compounds that chemisorb to the hydroxyl groups on zeolite surfaces.[12] This is frequently performed using chemical

vapor deposition (CVD) or chemical liquid deposition (CLD) techniques.[13−16] These methods enhance shape selectivity by narrowing surface pore openings and eliminating surface active sites; however, they also result in pore blockage and/or increased internal diffusion resistance due to pore mouth narrowing, which reduce molecular flux during sorption and separations and decrease catalytic activity.[17]

The aforementioned side effects of zeolite passivation can be circumvented by growing an epitaxial zeolite shell on the surface of a zeolite core with identical or congruent structure. Synthesis of core−shell (or layered) structures has been demonstrated for a wide range of inorganic and organic materials[18] with applications ranging from semiconductors[19,20] and drug delivery[21] to catalysis[22,23] and separations.[24] A key factor in the fabrication of zeolite core−shell composite structures is sufficient compatibility between core and shell in terms of framework composition, crystal structure, and synthesis conditions required to facilitate oriented or epitaxial growth of one crystal on the surface of another.[25] In the literature, many combinations of core−shell zeolites are reported, such as LTA@FAU,[26] SOD@CAN,[27] FAU@BEA,[28] MOR@MFI,[29] MFI@BEA,[30] and BEA@MFI.[31,32] These materials can be formed through heterogeneous nucleation and growth of the shell on the core. Alternatively, the shell layer can be formed through the use of nanocrystalline seeds that are first deposited on the core surface and then transformed into a contiguous layer via secondary growth.[33,34] One disadvantage of the latter approach is the need to calcine the seeded cores prior to shell growth in order to firmly fix the seeds to the core surface, a process that can introduce defects at the core/shell boundary.[35]

Herein, we focus on the formation of an MFI@MFI core−shell zeolite comprised of an aluminosilicate ZSM-5 (catalytically active) core and a siliceous silicalite-1 (catalytically benign) shell, both of which possess the same MFI crystal structure. Prior attempts to passivate MFI zeolite have resulted in incomplete silicalite-1 coverage, misaligned (nonepitaxial) shell growth, and/or individual silicalite-1 particles adhered to ZSM-5 seeds.[36−38] Core−shell MFI has been prepared by a one-step procedure using fluoride growth media;[39] however, the silicalite-1 shell thickness typically exceeds 1 μm and fluoride-based protocols are commercially restrictive. Prior examples have shown that MFI core−shell structures can improve catalyst selectivity, but often at the expense of reduced catalytic activity due to pore blockage or narrowing.[35] Moreover, structural mismatch between the core and shell can introduce molecular diffusion barriers that facilitate carbonaceous coke buildup.[40] Here, we report a robust protocol for realizing nanocrystalline ZSM-5@silicalite-1 with an ultrathin (<10 nm), epitaxial silicalite-1 shell of tunable thickness. Performance tests

using model reactions show that the shell layer preserves catalytic activity, thus avoiding pore blockage/narrowing and validating the overall effectiveness of this approach for zeolite design.

RESULTS AND DISCUSSION

Preparation of ZSM-5@Silicalite-1. ZSM-5 and its purely siliceous analogue silicalite-1 have an identical crystal structure (MFI type) comprised of 3-dimensional channels (ca. 5.5 Å diameter). ZSM-5 was synthesized according to a procedure reported by Persson et al.[41] with slight modifications. We prepared ZSM-5 crystals with a Si/Al molar ratio of 44, which was confirmed by inductively coupled plasma atomic emission spectroscopy (ICP-AES, Galbraith Laboratories). The crystal size was measured by dynamic light scattering (DLS) and electron microscopy. DLS analysis of a suspension of crystallites in aqueous solution revealed a relatively monodisperse distribution of crystals with a 156 nm average hydrodynamic diameter. Scanning electron microscopy (SEM) images of ZSM-5 confirmed their average size and size distribution (Figure 1A). High magnification SEM images (inset) revealed that crystals have rough surfaces comprised of spheroidal protrusions. ZSM-5 and other zeolites grow by nonclassical routes[42,43] involving the aggregation of amorphous precursors. For instance, Subotić and co-workers[44,45] suggest that ZSM-5 crystallization proceeds via a complex series of pathways involving (i) precursor aggregation, (ii) precursor disorder-to-order transitions, (iii) aggregate growth and coarsening, and (iv) densification of aggregates. Increased synthesis time often
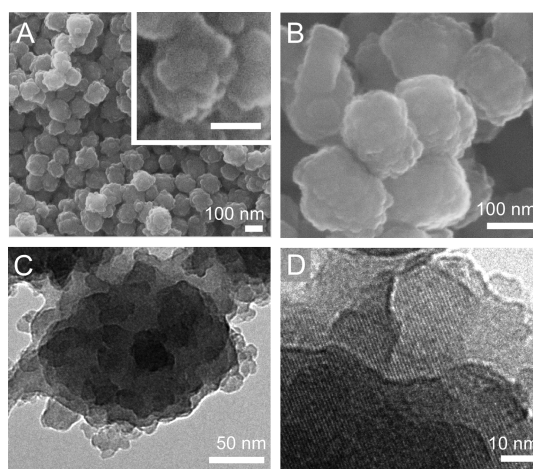

Figure 1. Electron microscopy images of ZSM-5 (core) and ZSM-5@silicalite-1 (core−shell) crystals prepared without thermal annealing. (A) SEM image of ZSM-5 crystals prepared at 100 °C for 60 h (inset scale bar = 100 nm). (B) SEM image of ZSM-5@silicalite-1 prepared with a 10 nm thick shell. (C) TEM image of a core−shell particle shows the rough crystal surface comprised of protrusions with sizes of ca. 5 to 20 nm. (D) HRTEM image of the core−shell particle reveals the presence of lattice fringes with translation symmetry extending from the exterior to the interior of the crystal.

leads to "annealing" by Ostwald ripening to form crystals with smooth surfaces. If syntheses are performed at low temperatures where the time scales for coarsening are sufficiently long, the final crystal is typically rough. There are many examples of highly corrugated crystals similar to the ones shown in Figure 1 where particles appear to be fractal aggregates of smaller crystallites or have surfaces comprised of protrusions with dimensions spanning 5 to 20 nm. Notable examples include the syntheses of LTA (zeolite A), FAU (zeolite X), and MFI (silicalite-1).[46−49]

An epitaxial layer of silicalite-1 was grown on ZSM-5 by seeded growth. During the synthesis of ZSM-5 seeds, the crystals were isolated by centrifugation and washed with deionized (DI) water to remove the supernatant. The crystals were then transferred as a gel (without drying) to a silicalite-1 growth solution. We used the gel transfer procedure to minimize ZSM-5 crystal aggregation and to prevent the potential alteration of its exterior surface that may occur upon drying. The silicalite-1 growth solution was prepared with tetraethylorthosilicate (TEOS) as the silica source and tetrapropylammonium (TPA$^+$) as an organic structure-directing agent (OSDA) to facilitate the formation of the MFI structure. We used a low supersaturated silica solution with molar composition x TEOS:14 TPAOH:9500 H_2O (with $x = 17-40$). The rationale for selecting a dilute concentration of silica was to minimize the homogeneous nucleation of silicalite-1, as well as achieve ultrathin (nanometer thick) silicalite-1 layers on the surface of ZSM-5 seeds. The silicalite-1 shell thickness was quantified by light scattering and electron microscopy. DLS measurements revealed that the hydrodynamic diameter increased by 10 nm or more depending on the TEOS concentration. The autocorrelation functions in DLS data showed no evidence of a bimodal size distribution that would be indicative of homogeneous silicalite-1 nucleation. SEM images of the core−shell particles (Figure 1B) revealed larger particles on average compared to the original seeds. Transmission electron microscopy (TEM) images indicated that the core−shell particles were rough (Figure 1C) with protrusions similar to those of the ZSM-5 core. High resolution TEM (HRTEM) revealed the presence of lattice fringes on the exterior surface (Figure 1D) with the same orientation as the particle interior, suggesting the shell formed *via* epitaxial growth of silicalite-1 on ZSM-5.

Rough surfaces impose challenges for the analysis of shell growth and the characterization of silicalite-1 uniformity on ZSM-5 crystals. In order to obtain definitive proof of a continuous epitaxial layer of silicalite-1, we prepared spheroidal ZSM-5 crystals with smoother surfaces that were more straightforward to characterize by scattering and microscopy techniques. This was accomplished by introducing an annealing step in the previous synthesis protocol. Following the completion of ZSM-5 crystallization, the gel product was
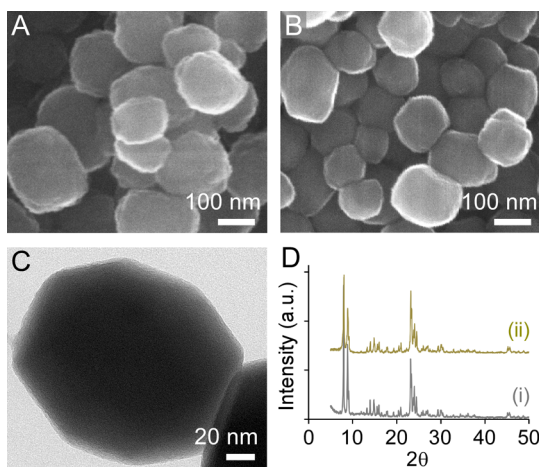

Figure 2. ZSM-5 (core) and ZSM-5@silicalite-1 (core−shell) crystals prepared with thermal annealing. (A) SEM image of ZSM-5 crystals after 170 °C annealing for 12 days. (B) SEM image of ZSM-5@silicalite-1 crystals after the growth of a 10 nm silicalite-1 layer and an additional 12 days of annealing at 170 °C. (C) TEM image of ZSM-5@silicalite-1 reveals crystals with smoother surfaces. (D) Powder XRD patterns of annealed (i) ZSM-5 and (ii) ZSM-5@silicalite-1 confirmed the formation of crystalline MFI. XRD data are offset along the y-axis for visual clarity.

transferred to a solution with molar composition 10 TEOS:14 TPAOH:9500 H_2O (with 1 wt % solid content) and was heated at 170 °C for 12 days. For this step, we selected a silica concentration that was approximately equal to the solubility of silicalite-1 in order to minimize ZSM-5 dissolution and prevent silicalite-1 crystallization. During hydrothermal annealing, protrusions on the exterior surfaces of ZSM-5 seed crystals coarsened, most likely as a result of Ostwald ripening, to produce crystals with smoother surfaces (Figure 2A). The annealed ZSM-5 seeds were then used to prepare ZSM-5@silicalite-1. Electron micrographs of the core−shell particles revealed a spheroidal morphology (Figure 2B) and showed no evidence of protrusions on their exterior surfaces (Figure 2C).

Powder X-ray diffraction (XRD) patterns of ZSM-5 (core) and ZSM-5@silicalite-1 (core−shell) confirmed that the products were fully crystalline (Figure 2D); *i.e.*, an amorphous peak in the region $2\theta = 20-30°$ was not observed in either the core or core−shell XRD patterns. ICP-AES analysis revealed Si/Al molar ratios of 44 and 53 for the core and core−shell samples, respectively. These results confirmed the expected increase in Si content due to shell growth. Moreover, N_2 adsorption measurements revealed that the BET surface area of ZSM-5 crystals (475 m^2/g) was approximately equal to the ZSM-5@silicalite-1 core−shell particles (454 m^2/g). These studies indicate that the silica layer on the surface of ZSM-5 is crystalline and that shell formation does not result in appreciable pore blockage (*i.e.*, the undesired outcome of many previously reported surface passivation techniques).

Validation of the Silicalite-1 Shell Structure. In order to confirm that the silica shell was a continuous epitaxial
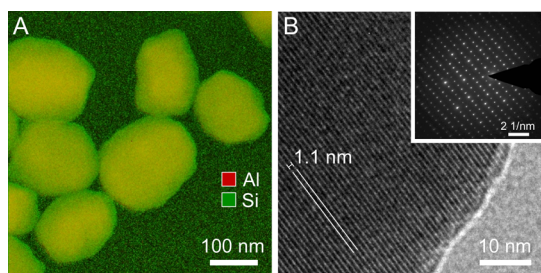
Figure 3. (A) Superimposed EFTEM mapping of annealed ZSM-5@silicalite-1 crystals prepared with a 10 nm silicalite-1 shell. The elements are color coded: Al (red) and Si (green). EDS line scans of core and core—shell particles are provided in Figure S7 of the SI. (B) HRTEM image of a core—shell crystal reveals the presence of lattice fringes that extend from the exterior to the interior of the particle without any discontinuity. The orientation of fringes (1.1 nm periodicity) is highlighted by the white lines. HRTEM images confirm the translational symmetry of pores between the core and shell due to the epitaxial growth of a silicalite-1 layer on the surface of ZSM-5 seeds. Inset: selected area electron diffraction (SAED) pattern of a core—shell particle reveals a single crystal (see also Figure S8 of the SI).

TABLE 1. Si/Al Ratios and Shell Thickness δ for H-ZSM-5 (Core) and H-ZSM-5@Silicalite-1 (Core—Shell)

	Si/Al ratio		
technique	core	core—shell	δ (nm)
XPS[a]	39	82	—
ICP-AES[a]	44	53	9
IPA-TPD[a,b]	45 ± 1	51 ± 2	7 ± 1
DLS	—	—	10 ± 2

[a] Experiments performed on H-form zeolites. [b] A 10% weight loss attributed to moisture within the zeolite during pretreatment is considered. Extra-framework Al estimated from ^{27}Al NMR (Table S1) is also included in the Si/Al ratio.

layer of silicalite-1, we used a combination of energy filtered transmission electron microscopy (EFTEM), electron dispersive spectroscopy (EDS), HRTEM, X-ray photoelectron spectroscopy (XPS), and catalytic testing with two probe reactions. EFTEM revealed the presence of a silica layer surrounding the ZSM-5 core with an approximately uniform thickness of *ca.* 10 nm (Figure 3A). The ZSM-5 core in EFTEM mappings appears to be yellow due to the superposition of Si (green) and Al (red) elements. Conversely, the exterior of the particle is green due to the presence of a Si-rich shell. EDS line scans along the cross sections of both core and core—shell particles reveal that Al is contained only within the core of ZSM-5@silicalite-1 (see Figure S7 of the Supporting Information, SI). HRTEM analysis of these particles shows the presence of lattice fringes (Figure 3B) and the translational symmetry of pores between the core and shell, as determined by the continuous orientation of lattice fringes without any apparent discontinuity at the core/shell interface. The continuous channels, which span from one end of the core—shell particle to the other, permit unhindered access of ions and molecules to diffuse within the 3D porous network of the MFI framework.

The formation of a thin silicalite-1 shell of thickness δ was confirmed by a combination of analytical techniques, summarized in Table 1. Calcined ZSM-5 and ZSM-5@silicalite-1 samples were activated to their proton forms (H-zeolites) prior to XPS and catalytic studies. XPS results indicate a significant increase in the Si/Al ratio after growth of the silicalite-1 shell. The fact that the Si/Al ratio of the ZSM-5@silicalite-1 sample significantly increases, but is still a finite value, indicates that the shell formed is very thin due to the short sampling depth of XPS (*i.e.*, on the order of nanometers). Comparison of the Si/Al ratios of ZSM-5

core particles reveals slight differences between ICP-AES and XPS. The Si/Al ratio provided by the latter is biased to the elemental composition near the exterior of the particle, whereas ICP-AES provides a bulk average elemental analysis. The lower Si/Al ratio from XPS measurements suggests the potential for so-called "Al zoning", a common phenomenon in ZSM-5 synthesis wherein crystallization leads to a Si/Al gradient that decreases in magnitude from the particle interior to its exterior.[50] It is important to point out, however, that high uncertainty in Si/Al ratios determined by XPS analysis have been reported in the literature for zeolites with low Al content such as these. Uncertainties in the Si/Al ratio as high as ±6 have been reported for zeolites with comparable Al content.[51] Other reports tend to use only qualitative comparisons when analyzing XPS data of zeolites with low elemental percentages of Al.[52] To this end, the quantitative degree of zoning in core (ZSM-5) particles cannot be conclusively determined from the XPS data.

Techniques such as temperature-programmed desorption (TPD) and ^{27}Al NMR provide additional means of analyzing the Al content in zeolite particles. The temperature-programmed desorption of isopropylamine (IPA-TPD) measures the Brønsted acid sites, which directly correlate with the tetrahedral (or framework) Al content in H-zeolites.[53,54] The extra-framework Al was quantified by ^{27}Al NMR (Figure 4) to be 9.1% for the core and 5.1% for core—shell, both of which are significantly lower than the percentages reported for commercial MFI catalysts (*i.e.*, values can reach as high as 25%).[55,56] The Si/Al data in Table 1 was used to estimate the shell thickness, δ, assuming a spherical morphology for all zeolite crystals. Knowing the Al content of the core and core—shell, the weight ratios of each were calculated, which is equivalent to volume ratio assuming the same density. The difference in volume for H-ZSM-5 (core) and H-ZSM-5@silicalite-1 (core—shell) was used to calculate the silicalite-1 shell thickness. The resulting δ values estimated from IPA-TPD and ICP-AES are comparable to DLS measurements (within experimental error), thus providing additional evidence of a thin silicalite-1 shell.
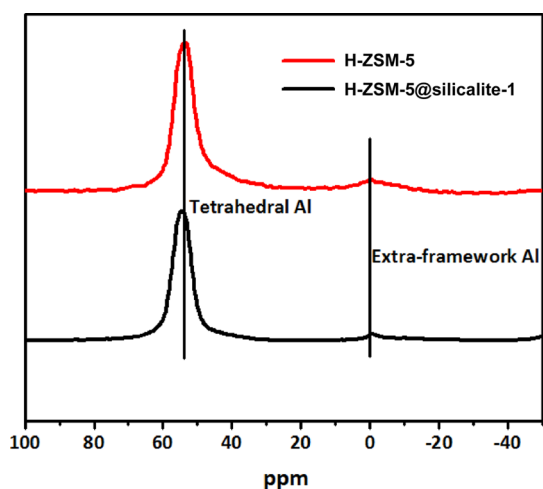
Figure 4. ^{27}Al NMR was used to quantify the amount of extra-framework alumina in H-ZSM-5 (core) and H-ZSM-5@silicalite-1 (core−shell). The intensities at 60 and 0 ppm correspond to framework and extra-framework alumina, respectively.

Figure 5. Gas phase turnover frequency (TOF) in a flow reactor of (A) triisopropylbenzene and (B) acetic acid over H-ZSM-5@silicalite-1 prepared with a 10 nm silicalite-1 shell, as well as the H-ZSM-5 core. The reactions were performed at 1 atm after pretreating the catalyst in He flow at 300 °C for 1 h to remove physisorbed water from the catalyst surface. Cracking of triisopropylbenzene (A) was done at 400 °C and ketonization of acetic acid (B) was done at 320 °C. The outlet stream from the flow reactor was connected to a GC-FID equipped with an innowax column to quantify the products. The number of Brønsted sites was estimated *via* IPA-TPD (excluding extra-framework Al from ^{27}Al NMR). Error bars represent two standard deviations.

Two probe chemical reactions were used to confirm the surface passivation of H-ZSM-5 and the unhindered access to Brønsted acid sites within H-ZSM-5@silicalite-1. Triisopropylbenzene (TIPB) is a bulky molecule with three reactive isopropyl groups and a kinetic diameter of 8.5 Å, which is larger than the pores of MFI (5.5 Å). This limits the reactivity of TIPB to the external surface of the zeolite.[57−59] The second probe molecule selected for this study was acetic acid, which reacts *via* decarboxylative ketonization over Brønsted sites in zeolites to produce acetone.[60] The kinetic diameters of acetic acid and the reaction products (acetone, CO_2 and H_2O) are small enough to diffuse through the micropores of MFI. Figure 5A shows a dramatic reduction in the reactivity of TIPB over H-ZSM-5@silicalite-1 when compared to H-ZSM-5. On an equivalent acid site basis, the surface activity is limited to less than 6% of the activity of the parent zeolite, indicating a near complete silicalite-1 coating on H-ZSM-5. The removal of external surface Brønsted acid sites in H-ZSM-5@silicalite-1 was also demonstrated by infrared (IR) spectroscopy of an adsorbed bulky pyridine, ditertbutylpyridine (see Figure S4 of the SI). A signal at 1616 cm^{-1}, corresponding to protonation of ditertbutylpyridine,[61,62] is observed for the core, with little to no peak in this region for the core−shell sample, indicating the absence of external Brønsted acid sites. The rate of acetic acid conversion normalized per total acid site, as shown in Figure 5B, is identical for the samples with and without a silicalite-1 shell. The rate of catalyst deactivation as a function of time is identical for both catalysts as well. This identical catalytic activity after incorporating the silicalite-1 shell demonstrates that the internal acid sites are accessible for this reaction, which is consistent with the results from HRTEM and BET analysis. This finding also confirms our ability to passiv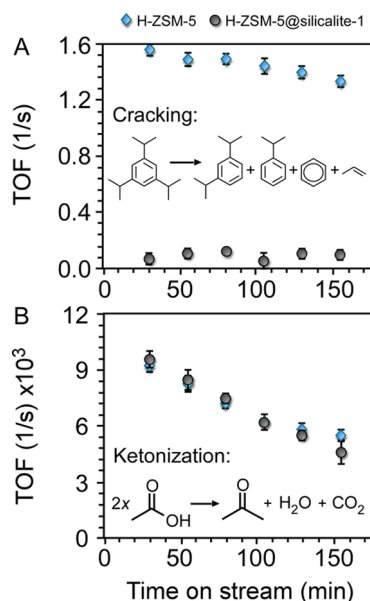ate ZSM-5 surfaces without hindering the intrinsic activity of the catalyst, which is a significant advancement in zeolite core−shell design.

Tailoring the Silicalite-1 Shell Thickness. We investigated two approaches to tune the shell thickness. The synthesis can either be quenched at a specific time of hydrothermal treatment to achieve the desired thickness (leaving a fraction of unreacted silica in the growth solution), or an exact concentration of TEOS can be selected such that shell growth is terminated once the solution reaches thermodynamic equilibrium (*i.e.*, silicalite-1 solubility). We carried out the first approach and monitored the rate of shell growth using *ex situ* DLS measurements of ZSM-5@silicalite-1 particles that were heated for various times in a silicalite-1 growth solution. In order to measure shell growth over a reasonable time scale, we used a silicalite-1 growth solution with lower pH (molar composition 14 TEOS:7 TPAOH: 9500 H_2O), which increases the rate of crystallization. As shown in Figure 6, DLS measurements revealed a monotonic increase in the hydrodynamic diameter of ZSM-5@silicalite-1 with heating time. The linear rate of silicalite-1 growth is consistent with trends in the literature.[63] The measured growth rate of 3.8 nm/h (*i.e.*, change in hydrodynamic diameter with time) is approximately equal to the 4.0 nm/h value reported by Li *et al.*[64] in their study of silicalite-1 growth at similar conditions. CONTIN analysis[65,66] of the DLS
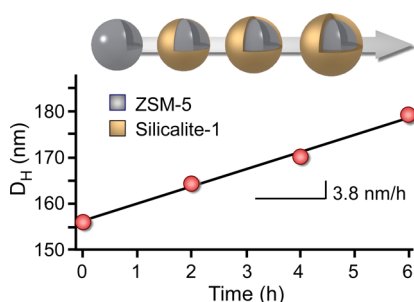
Figure 6. *Ex situ* DLS measurements of ZSM@silicalite-1 growth. The temporal change in hydrodynamic diameter D_H was analyzed by heating a 1 wt % dispersion of ZSM-5 seeds (D_H = 156 nm) in a silicalite-1 growth solution with molar composition 14 TEOS:7 TPAOH:9500 H_2O. Samples were removed from the oven (100 ± 1 °C) at periodic times and were quenched to room temperature for DLS analysis. The symbols are an average of three measurements with standard deviation of ±2 nm (less than the size of the symbols). The slope of linear regression (solid line) reveals a 3.8 nm/h rate of silicalite-1 growth.

autocorrelation functions revealed a single particle size distribution for all extracted samples, which suggests that homogeneous silicalite-1 nucleation and crystal growth is negligible. Indeed, if the latter were to occur with any appreciable frequency, we would anticipate the presence of a bimodal size distribution. The absence of a smaller particle size population in the DLS data suggests that ZSM-5@silicalite-1 growth is the dominant pathway.

A disadvantage of the previous approach is that silicalite-1 growth is terminated prior to reaching silicalite-1 solubility. As such, TEOS is wasted in this process and the extraction of crystals from the supernatant could lead to the potential deposition of amorphous silica from solution to the exterior surfaces of ZSM-5@silicalite-1 (thereby leading to pore blockage). An alternative, and more practical approach, is to select the exact amount of TEOS needed to achieve the desired thickness, such that silicalite-1 growth is terminated once equilibrium is reached. The ability to control the thickness of the silicalite-1 shell, however, requires knowledge of solution chemistry and the approximate solubility of MFI crystals. Prior studies have shown that silicalite-1 growth solutions prepared with TEOS are comprised of silica nanoparticle precursors (1−6 nm) that self-assemble at a critical aggregation concentration (CAC), which is defined by the silica concentration at a 1:1 molar ratio of x TEOS:y TPAOH.[67,68] The kinetic phase diagram for silicalite-1 growth solutions depicted in Figure 7A reveals the presence of two distinct regions divided by the CAC (solid line). Region I (x/y < 1) consists of soluble silica species (*i.e.*, silicic acid and silica oligomers), while region II (x/y > 1) consists of silica molecules in quasi-equilibrium with silica nanoparticles. There have been many studies that focused on characterizing the physicochemical properties of silica nanoparticles and identifying their putative role(s) in silicalite-1
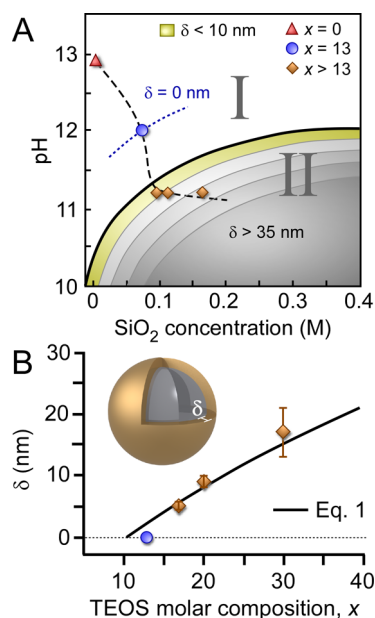

Figure 7. (A) The kinetic phase diagram of silicalite-1 growth solutions is divided into two distinct sections: Region I contains soluble silica (monomers and oligomers) and Region II is comprised of soluble species in quasi-equilibrium with silica nanoparticle precursors.[74] The CAC (solid line) divides the two regions. The pH was measured for solutions of molar composition x TEOS:14 TPAOH:9500 H_2O where x > 13 (orange diamonds) was used for shell growth, x = 13 (blue circle) is an estimate of the silicalite-1 solubility c_e, and x = 0 (red triangle) is a silica-free solution. The dashed line is interpolated between experimental data points and the dotted line is the estimated shell thickness δ = 0 nm. The color coded segments in Region II illustrate the progressive increase in δ with increased silica super-saturation. Ultrathin layers are formed near the CAC (yellow region, δ < 10 nm). (B) The shell thickness of ZSM-5@silicalite-1 can be tailored by adjusting the molar composition of TEOS. Growth solutions with ZSM-5 crystals (0.01 g seeds per 1 g solution) were heated for 24 h at 100 °C, followed by 12 days of annealing at 170 °C. The solid line corresponds to eq 1 where c_e = 0.06 M (x ≈ 10) and x/c = 171 L mol^{-1}. Data points are the average of 3 measurements and error bars equal two standard deviations.

crystallization.[69−73] During the course of silicalite-1 crystallization, silica molecules and nanoparticles in the growth solution are progressively consumed, resulting in a temporal shift from right to left along the dashed line in Figure 7A. The final stage of silicalite-1 growth involves an exothermic-to-endothermic transition in the heat of crystallization when crossing the CAC that is accompanied by an increase in pH.[74] Crystal growth is complete once the concentration of silica in solution reaches the thermodynamic solubility of silicalite-1 (estimated as the dotted line in Figure 7A).

The design of ZSM-5@silicalite-1 must take into account the relative concentrations of ZSM-5 seeds and TEOS. We used a concentration of 2.5 × 10^{15} seeds/L growth solution (*i.e.*, N = 6.3 × 10^{13} seeds). If the concentration of seeds is sufficiently low, there is a higher probability of silicalite-1 nucleation and growth occurring in solution rather than on the surface of ZSM-5 seeds. This would lead to a mixture of ZSM-5,

silicalite-1, and/or ZSM-5@silicalite-1 crystals in the final product. There is evidence in the literature[75] that suggests silicalite-1 crystallites can attach to the surface of ZSM-5 crystals, thus generating fractal aggregates as opposed to a continuous epitaxial silicalite-1 shell. Depending on the size of silicalite-1 crystals and their coverage on ZSM-5 surfaces, these layers may appear to be a uniform shell that would go undetected by cursory inspection using bulk characterization techniques such as DLS or SEM, whereas higher resolution techniques, such as TEM, are capable of discerning these differences.

The preparation of ZSM-5@silicalite-1 with predictable shell thickness also requires the selection of an appropriate silica supersaturation. To this end, we prepared several growth solutions of varying silica concentration and measured the resulting shell thickness δ (Figure 7B). For these studies we used $0.09-0.2$ M SiO_2 to adjust δ between 5 and 30 nm. We observed a monotonic increase in δ with silica concentration that enables the silicalite-1 layer to be selectively tuned. Molecular layers of silica ($\delta < 2$ nm) can be achieved by working at lower silica concentrations; however, for the purpose of this study, we used an appreciable shell thickness (*ca*. 10 nm) in order to confirm silicalite-1 growth on ZSM-5 seeds. The shell thickness can be adjusted using eq 1 with the judicious selection of silica concentration c for seeded crystallization:

$$c(\delta, T, \mathrm{pH}) = \frac{4\pi N \rho_{SiO_2}}{3 V M_{SiO_2}} \left((R+\delta)^3 - R^3 \right) + c_e(T, \mathrm{pH}) \quad (1)$$

The parameter R is the average radius of ZSM-5 seeds, N is the number of crystal seeds, ρ is density of silicalite-1, V is the total volume of the growth solution, M is molar mass of SiO_2, and c_e is the silica concentration at silicalite-1 solubility. The value of c_e establishes a lower limit of TEOS concentration for the preparation of ZSM-5@silicalite-1. When $c = c_e$ the solution is at equilibrium and there is no growth of silicalite-1 (*i.e.*, $\delta = 0$ nm), whereas $c > c_e$ leads to the formation of a silicalite-1 shell. Without *a priori* knowledge of c_e, we used this parameter to fit the experimental data in Figure 7B assuming 2.0 g/cm^3 as the silicalite-1 density and 78 nm as the average radius of ZSM-5 seeds. A value of $c_e = 0.06 \pm 0.01$ M (Figure 7B, solid line) provided the best fit. To validate this estimate of c_e, we first

measured the pH of a seeded growth solution after 24 h of heating when the silicalite-1 shell was fully grown and the solution reached solubility. We then prepared nonseeded growth solutions by varying the molar composition x TEOS:14 TPAOH: 9500 H_2O until the seeded and nonseeded solutions had similar pH (11.8 and 12.0, respectively). This occurred at $x = 13$ or $c_e = 0.07$ M SiO_2 (Figure 7, blue circles), which is comparable to the silicalite-1 solubility from eq 1.

CONCLUSIONS

In summary, we have demonstrated an ability to synthesize a core–shell zeolite with compositionally distinct, but structurally identical domains. For this study we selected the MFI framework structure, which is one of the most commercially relevant zeolites in heterogeneous catalysis. Using a broad combination of experimental techniques, we have shown that ZSM-5@silicalite-1 can be prepared with tunable shell thickness. Electron microscopy and textural analysis confirmed that silicalite-1 forms an epitaxial layer on ZSM-5 crystals without blocking pore openings. SEM and DLS were used in combination to confirm that the shell thickness can be tailored with nanometer resolution. XPS, EDS, and TPD measurements revealed the presence of a siliceous shell, while probe reactions using molecules that were either too large or adequately sized to access MFI pores confirmed the uniform shell coverage. Moreover, these studies revealed that the activity of ZSM-5 catalysts is not compromised by the overgrowth of a passivation layer. This finding highlights a distinct advantage of our synthetic protocol relative to alternative techniques that have been used to passivate zeolite surfaces.

The synthesis of ZSM-5@silicalite-1 offers a pathway for tuning the physicochemical properties of MFI-type materials. The generation of passivation layers is particularly beneficial for heterogeneous catalysis where the inactive shell enhances product selectivity. Knowledge of solution chemistry for aluminosilicate zeolites and their siliceous analogues affords the opportunity to selectively design novel materials with tailored properties. To this end, the method described here may prove to be a general platform for core–shell design that could potentially be applied to other zeolite frameworks.

EXPERIMENTAL SECTION

Materials. The following chemicals were purchased from Sigma-Aldrich: tetraethylorthosilicate (TEOS, 98%), aluminum isopropoxide (98%), sodium hydroxide pellets (NaOH, 98%), 1,3,5-tri-isopropyl-benzene (TIPB, 95%), acetic acid (ACS reagent, ≥99.7%), isopropylamine (IPA >99.5%), and 2,6-ditertbutylpyridine (DTBP, >97%). Tetrapropylammonium hydroxide (TPAOH, 40%) was purchased from Alfa Aesar.

The deionized (DI) water used for all synthesis and analytical measurements was purified with an Aqua Solutions RODI-C-12A purification system (18.2 MΩ). All gases necessary for reactions and gas chromatography analysis (He, N_2, H_2, and air) were obtained from Airgas. The N_2 for textural analysis was obtained from Praxair.

Synthesis of ZSM-5 Seeds. Growth solutions were prepared with a molar composition of 6 TPAOH:0.1 Na_2O:25 SiO_2:0.25

Al$_2$O$_3$:480 H$_2$O:100 EtOH. We first added TEOS dropwise to a solution of TPAOH, NaOH, and DI water (25 mL total volume). This solution was stirred overnight at room temperature. Aluminum isopropoxide was added and the mixture was aged for an additional 24 h at room temperature with continuous stirring. The solution was then placed in an acid digestion bomb (Parr Instruments) and was heated in a ThermoFisher Precision 3050 Series gravity oven at 100 °C. The solution was removed after 60 h and immediately cooled to room temperature. The crystalline product was isolated from the supernatant by three centrifugation and washing cycles of the mother liquor with DI water at 13 000 rpm for 40 min. The water was decanted, leaving behind a gel containing the ZSM-5 crystals. For protocols without an annealing step, a portion of the ZSM-5 gel was removed and dried in air for further characterization, while the remaining gel was directly added to a silicalite-1 growth solution (without drying) to prepare core–shell particles. For protocols employing an annealing step, the entire ZSM-5 gel was transferred to a solution with composition 10 TEOS:14 TPAOH:9500 H$_2$O. This solution was prepared by adding an appropriate amount of TEOS (dropwise) to a solution containing TPAOH and DI water (25 mL total volume). The solution was stirred at room temperature overnight prior to the addition of ZSM-5 seed crystals (1 wt %). The solution containing ZSM-5 seeds was thoroughly mixed, placed in an acid digestion bomb, and heated for 12 days at 170 °C. The solution was removed from the oven and cooled to room temperature. A similar centrifugation/washing procedure was used to isolate the ZSM-5 crystals as a gel, which was fully transferred to a silicalite-1 growth solution (without drying).

Synthesis of ZSM-5@Silicalite-1. A layer of silicalite-1 was grown on ZSM-5 seeds using a growth solution with a molar composition of x TEOS:14 TPAOH:9500 H$_2$O (with x = 17–40). This solution was prepared by adding an appropriate amount of TEOS (dropwise) to a solution containing TPAOH and DI water (25 mL total volume). The solution was stirred at room temperature overnight. Shell growth was carried out by adding ZSM-5 seeds (1 wt %) to the silicalite-1 growth solution. Prior to hydrothermal treatment, the solution pH was measured using an Orion 3-star Plus pH benchtop meter and 8102BNUWP ROSS Ultra electrode. The suspension was placed in an acid digestion bomb and heated for 24 h at 100 °C. The solution was removed from the oven and cooled to room temperature. A similar centrifugation/washing procedure was used to isolate ZSM-5@silicalite-1 crystals as a gel. For protocols without an annealing step, the entire gel was dried in air for further characterization. For processes employing an annealing step, the gel was directly transferred (without drying) to a solution with composition 10 TEOS:14 TPAOH:9500 H$_2$O, which was heated for 12 days at 170 °C. The solution was then removed from the oven, the solid was isolated as a gel by centrifugation and washing, and the product was dried in air for further analysis.

Preparation of H-Zeolites. ZSM-5 and ZSM-5@silicalite-1 samples were calcined to remove occluded TPA$^+$ from the pores using a ThermoScientific Lindberg Blue M tubular furnace. Calcination was performed with a temperature ramp rate of 1 °C/min and a dwell time of 5 h at 550 °C under the constant flow of compressed air (190 mL/min). An appropriate amount of each sample was then mixed with DI water to yield a 5 wt % suspension. This suspension was heated at 70 °C for 12 h, and washed with DI water by centrifugation and decanting, such that the pH of the supernatant was within the range 6 to 7. The precipitate was mixed with a 1.0 M ammonium nitrate solution to yield a 5 wt % suspension. This suspension was then heated at 80 °C for 5 h to allow the exchange of extra-framework Na$^+$ ions with NH$_4^+$. The solid material was recovered by centrifugation. This entire process was performed for a total of three cycles, and the final product was dried at room temperature and calcined at the same condition as above. The resulting H-form zeolite samples were used for BET, XRD, XPS, IPA-TPD, probe reactions, and ditertbutylpyridine adsorption experiments.

Materials Characterization. The MFI crystal structure of core and core–shell samples was verified by powder X-ray diffraction (XRD) using a Siemens D5000 X-ray diffractometer with Cu Kα radiation (40 kV, 30 mA, λ = 1.54 Å). The elemental composition of zeolite samples was determined by inductively coupled plasma atomic emission spectroscopy (ICP-AES) at Galbraith Laboratories (Knoxville, TN). The BET surface area of H-zeolite samples was measured by N$_2$ adsorption using a Micromeritics ASAP2020 instrument. Crystal morphology, size, and particle size distribution were assessed by scanning electron microscopy (SEM) using a FEI model Strata235 instrument. To prepare SEM samples, a small amount of the zeolite aqueous suspension was placed on a glass slide and dried overnight. The crystals were then transferred onto carbon grids and coated with a thin layer of carbon (ca. 30 nm). Transmission electron microscopy (TEM) was performed at the Texas A&M University Microscopy and Imaging Center. TEM specimens were prepared by dispersing zeolite particles in ethanol with sonication. A small droplet of the dispersion was placed on a TEM grid and dried with a filter paper. HRTEM, SAED, and EDS data were obtained with a Super-Twin TEM fitted with a Schottky field emission gun, a 2 k × 2 k Gatan CCD camera, and an EDS detector. EFTEM data was obtained using a FEI Tecnai G2 F20 ST FE-TEM instrument.

X-ray photoelectron spectroscopy (XPS) analysis of samples was performed using a PHI 5800 ESCA (Physical Electronics) multitechnique system equipped with a standard achromatic Al Kα X-ray source (1486.6 eV) operating at 300 W (15 kV and 20 mA) and a concentric hemispherical analyzer. The samples were filled in the specimen holder and outgassed in the introduction chamber prior to analysis. Survey spectra (0–1400 eV) and high-resolution spectra were collected with a pass energy of 187.85 and 23.50 eV, respectively. All data were collected at a 45° takeoff angle. To compensate for surface charging effects, all spectra were referenced to the hydrocarbon C 1s peak at 284.6 eV.

Growth solutions for dynamic light scattering (DLS) measurements were prepared with molar composition 14 TEOS:7 TPAOH:9500 H$_2$O (pH = 10.8) using the same protocol for silicalite-1 synthesis. To this solution was added an aliquot of stock ZSM-5 seed solution (3 g zeolite in 19 mL DI water) in the amount of 5 g of seed solution per 75 g of growth solution. After 30 min of stirring, the mixture was divided equally into three acid digestion bombs, and placed in an oven regulated at 100 °C. At various time points, a sample was removed from the oven, quenched to room temperature, filtered through a 0.45 mm nylon membrane (Pall Corp.), and diluted to obtain a transparent solution prior to DLS measurements. The degree of dilution was adjusted to ensure equal scattering count rates for each sample. Samples labeled as the zero time point refer to the solution without any heating. A total of three DLS measurements were taken for each sample (2 min per measurement) to obtain an average crystal size and standard deviation. Autocorrelation functions were analyzed using the method of cumulants to obtain an average hydrodynamic diameter. All measurements were performed using a Brookhaven Instruments BI-200SM machine equipped with a TurboCorr Digital Correlator, a HeNe laser (637 nm), and a refractive index matching decalin bath. The temperature of the DLS sample was regulated at 25 °C.

The ^{27}Al NMR experiments were performed on a Bruker AVIII HD NMR spectrometer operating at a magnetic field strength of 11.74 T, equipped with a 4 mm Bruker MAS probe. For the MAS experiments of ^{27}Al (130.3754 MHz), a single pulse acquisition was applied with a spinning speed of 14 kHz and a short RF pulse (less than 15°) with a recycle delay of 0.5–1 s. Spectra were collected after 10240 scans and referenced to AlCl$_3$ (aq. 1 M) at 0 ppm.

Material Testing in a Fixed Bed Reactor. Flow reaction studies were performed in a quartz tube reactor (1/4" OD) at 400 °C and at atmospheric pressure. The H-zeolite catalyst was diluted with acid washed glass beads packed in the reactor between plugs of quartz wool. The inlet of the reactor was heated to create a vaporization zone and the outlet stream of the reactor as well as the six port valve for injection to the gas chromatograph (GC) were heated to 250 °C to prevent condensation. The temperature of the catalyst bed was controlled by a thermocouple attached to the outer wall of the reactor. The catalyst was preheated and flushed with helium (50 mL/min) for 1 h at

400 °C before introducing the reactant *via* a syringe pump. The results and product distribution were analyzed using a HP-6890GC gas chromatograph (GC) equipped with a flame ionization detector (FID) and innowax column (30 m and 0.25 μm). Reaction products were condensed in a sample bubbler using ice and water as a coolant medium for identification *via* GCMS.

For temperature-programmed desorption (TPD) experiments, 50 mg of H-zeolite sample was packed in a quartz reactor (1/4″ OD) between two quartz plugs and flushed at 400 °C for 1 h with helium as the carrier gas (50 mL/min). After pretreatment, the temperature was reduced to 100 °C and 2 μL pulses of isopropylamine (IPA) were injected into the reactor through a septum using a syringe. The IPA exiting the reactor was tracked by following species with a mass-to-charge ratio (*m/z*) of 58 using a MKS Cirrus 200 quadrupole mass spectrometer (MS) until the signal remained constant with additional pulses to ensure that all of the acid sites in the catalyst bed were saturated. After adsorption of IPA on to the catalyst bed, it was flushed with carrier gas at 20 mL/min and 100 °C for 4 h to remove any physically absorbed IPA, after which the temperature was ramped from 100 to 600 °C at a rate of 10 °C/min under a flow of He (20 mL/min). The outlet stream of the reactor was connected to the MS to analyze the desorbing species from the catalyst bed. Quantification of the number of moles of product evolved in the MS was conducted by injecting standards, with propylene gas injected through a sample loop. The Brønsted acid sites for each H-zeolite sample were quantified by integrating the moles of propylene (*m/z* = 41) desorbed during the IPA-TPD experiment.

Flow reaction studies of TIPB were performed at 400 °C and atmospheric pressure, keeping the *W/F* = 0.2 h, where *W* is the total mass of catalyst (g-zeolite) and *F* is the reactant feed rate (g-reactant h⁻¹). The acetic acid ketonization reaction was performed at 320 °C and atmospheric pressure with *W/F* = 0.3 h. Reactant and helium (carrier gas) feed rates for the probe reactions were 0.1 and 50 mL/min, respectively. For all reactions, the catalyst was first preheated and flushed with helium (50 mL/min) for 1 h at 400 °C prior to introducing the reactant *via* a syringe pump.

Adsorption measurements with DTBP were conducted in a PerkinElmer Spectrum 100 FT-IR Spectrometer equipped with a Harrick Praying Mantis chamber. After pretreating the H-zeolite sample at 300 °C in helium flow for 1 h, the temperature was reduced to 50 °C and a blank spectrum of the zeolite surface was taken as a reference. DTBP was then adsorbed onto the surface for 30 min at 50 °C through a sample bubbler maintained at −7 °C while flowing helium at a rate of 50 mL/min (using a Porter mass flow controller). This was followed by flushing for 2 h at 50 °C under a flow of 50 mL/min to remove physically adsorbed DTBP. After flushing, the spectrum of the H-zeolite surface adsorbed with DTBP was collected at 50 °C and then the temperature was raised at a steady rate of 10 °C/min. Analysis at each desired temperature was conducted by stopping the ramp and holding at a fixed temperature to obtain the spectrum (64 scans) prior to continuing the temperature ramp.

Conflict of Interest: The authors declare no competing financial interest.

Supporting Information Available: XRD patterns of calcined ZSM-5 samples (both annealed and nonannealed) with a simulated reference pattern; BET curves of annealed core and core−shell; a representative DLS autocorrelation function and CONTIN histogram for the 6 h sample; XPS results; IPA TPD spectra; ²⁷Al NMR analysis; ditertbutylpyridine IR data of core and core−shell H-form catalysts; and EDS and SAED data from electron microscopy. This material is available free of charge *via* the Internet at http://pubs.acs.org.

REFERENCES AND NOTES

1. Kim, K.; Ryoo, R.; Jang, H. D.; Choi, M. Spatial Distribution, Strength, and Dealumination Behavior of Acid Sites in Nanocrystalline MFI Zeolites and Their Catalytic Consequences. *J. Catal.* **2012**, *288*, 115–123.
2. Seo, Y.; Cho, K.; Jung, Y.; Ryoo, R. Characterization of the Surface Acidity of MFI Zeolite Nanosheets by P-31 NMR of Adsorbed Phosphine Oxides and Catalytic Cracking of Decalin. *ACS Catal.* **2013**, *3*, 713–720.
3. Rollmann, L. D. US4088605, 1978.
4. Chang, C. D.; Rodewald, P. G. US5475179, 1995.
5. Wichterlová, B.; Čejka, J. A Comparison of the Ethylation of Ethylbenzene and Toluene on Acid, Cationic and Silylated ZSM-5 Zeolites. *Catal. Lett.* **1992**, *16*, 421–429.
6. Bartholomew, C. H. Mechanisms of Catalyst Deactivation. *Appl. Catal., A* **2001**, *212*, 17–60.
7. Corbin, D. R.; Schwarz, S.; Sonnichsen, G. C. Methylamines Synthesis: A Review. *Catal. Today* **1997**, *37*, 71–102.
8. Foster, A. J.; Jae, J.; Cheng, Y. T.; Huber, G. W.; Lobo, R. F. Optimizing the Aromatic Yield and Distribution from Catalytic Fast Pyrolysis of Biomass over ZSM-5. *Appl. Catal., A* **2012**, *423*, 154–161.
9. Kwak, B. S.; Sung, J. Skeletal Isomerization of 1-Butene over Surface Modified Ferrierite Catalysts. *Catal. Lett.* **1998**, *53*, 125–129.
10. Yan, Z. M.; Ding, M. A.; Zhuang, J. Q.; Liu, X. C.; Liu, X. M.; Han, X. W.; Bao, X. H.; Chang, F. X.; Xu, L.; Liu, Z. M. On the Acid-Dealumination of USY Zeolite: A Solid State NMR Investigation. *J. Mol. Catal. A: Chem.* **2003**, *194*, 153–167.
11. Zheng, S. R.; Jentys, A.; Lercher, J. A. On the Enhanced Para-Selectivity of HZSM-5 Modified by Antimony Oxide. *J. Catal.* **2003**, *219*, 310–319.
12. Choplin, A. Surface Organometallic Chemistry on Zeolites—A Tool for Modifying the Sorption Properties of Zeolites. *J. Mol. Catal.* **1994**, *86*, 501–512.
13. Cheng, Y. T.; Wang, Z. P.; Gilbert, C. J.; Fan, W.; Huber, G. W. Production of *p*-Xylene from Biomass by Catalytic Fast Pyrolysis Using ZSM-5 Catalysts with Reduced Pore Openings. *Angew. Chem., Int. Ed.* **2012**, *51*, 11097–11100.
14. Niwa, M.; Kato, S.; Hattori, T.; Murakami, Y. Fine Control of the Pore-Opening Size of the Zeolite Mordenite by Chemical Vapor Deposition of Silicon Alkoxide. *J. Chem. Soc., Faraday Trans. 1* **1984**, *80*, 3135–3145.
15. Tominaga, K.; Maruoka, S.; Gotoh, M.; Katada, N.; Niwa, M. HZSM-5 Modified by Silica CVD for Shape-Selective Production of *p*-Xylene: Influence of *In Situ* and *Ex Situ* Preparation Conditions of the Zeolite. *Microporous Mesoporous Mater.* **2009**, *117*, 523–529.
16. Weber, R. W.; Fletcher, J. C. Q.; Möller, K. P.; O'Connor, C. T. The Characterization and Elimination of the External Acidity of ZSM-5. *Microporous Mater.* **1996**, *7*, 15–25.
17. Zheng, S.; Heydenrych, H. R.; Roger, H. P.; Jentys, A.; Lercher, J. A. On the Enhanced Selectivity of HZSM-5 Modified by Chemical Liquid Deposition. *Top. Catal.* **2003**, *22*, 101–106.
18. Chaudhuri, R. G.; Paria, S. Core/Shell Nanoparticles: Classes, Properties, Synthesis Mechanisms, Characterization, and Applications. *Chem. Rev.* **2012**, *112*, 2373–2433.
19. Dabbousi, B. O.; Rodriguez-Viejo, J.; Mikulec, F. V.; Heine, J. R.; Mattoussi, H.; Ober, R.; Jensen, K. F.; Bawendi, M. G. (CdSe)ZnS Core−Shell Quantum Dots: Synthesis and Characterization of a Size Series of Highly Luminescent Nanocrystallites. *J. Phys. Chem. B* **1997**, *101*, 9463–9475.
20. Reiss, P.; Protiere, M.; Li, L. Core/Shell Semiconductor Nanocrystals. *Small* **2009**, *5*, 154–168.
21. Zhu, Y. F.; Shi, J. L.; Shen, W. H.; Dong, X. P.; Feng, J. W.; Ruan, M. L.; Li, Y. S. Stimuli-Responsive Controlled Drug Release from a Hollow Mesoporous Silica Sphere/Polyelectrolyte Multilayer Core−Shell Structure. *Angew. Chem., Int. Ed.* **2005**, *44*, 5083–5087.

22. Alayoglu, S.; Nilekar, A. U.; Mavrikakis, M.; Eichhorn, B. Ru-Pt Core–Shell Nanoparticles for Preferential Oxidation of Carbon Monoxide in Hydrogen. *Nat. Mater.* **2008**, *7*, 333–338.

23. Zhang, X.; Su, Z. H. Polyelectrolyte-Multilayer-Supported Au@Ag Core–Shell Nanoparticles with High Catalytic Activity. *Adv. Mater.* **2012**, *24*, 4574–4577.

24. Kim, W. G.; Zhang, X. Y.; Lee, J. S.; Tsapatsis, M.; Nair, S. Epitaxially Grown Layered MFI–Bulk MFI Hybrid Zeolitic Materials. *ACS Nano* **2012**, *6*, 9978–9988.

25. Ji, Y. J.; Zhang, B.; Xu, L.; Wu, H. H.; Peng, H. G.; Chen, L.; Liu, Y. M.; Wu, P. Core/Shell-Structured Al-MWW@B-MWW Zeolites for Shape-Selective Toluene Disproportionation to *para*-Xylene. *J. Catal.* **2011**, *283*, 168–177.

26. Porcher, F.; Dusausoy, Y.; Souhassou, M.; Lecomte, C. Epitaxial Growth of Zeolite X on Zeolite A and Twinning in Zeolite A: Structural and Topological Analysis. *Mineral. Mag.* **2000**, *64*, 1–8.

27. Okubo, T.; Wakihara, T.; Plevert, J.; Nair, S.; Tsapatsis, M.; Ogawa, Y.; Komiyama, H.; Yoshimura, M.; Davis, M. Hetero-epitaxial Growth of a Zeolite. *Angew. Chem., Int. Ed.* **2001**, *40*, 1069.

28. Zheng, J. J.; Zhang, X. W.; Wang, Y.; Bai, Y. D.; Sun, W. F.; Li, R. F. Synthesis and Catalytic Performance of a Bi-Phase Core–Shell Zeolite Composite. *J. Porous Mater.* **2009**, *16*, 731–736.

29. Bouizi, Y.; Rouleau, L.; Valtchev, V. P. Bi-Phase MOR/MFI-Type Zeolite Core–Shell Composite. *Microporous Mesoporous Mater.* **2006**, *91*, 70–77.

30. Bouizi, Y.; Rouleau, L.; Valtchev, V. P. Factors Controlling the Formation of Core–Shell Zeolite-Zeolite Composites. *Chem. Mater.* **2006**, *18*, 4959–4966.

31. Bouizi, Y.; Diaz, I.; Rouleau, L.; Valtchev, V. P. Core–Shell Zeolite Microcomposites. *Adv. Funct. Mater.* **2005**, *15*, 1955–1960.

32. Pirngruber, G. D.; Laroche, C.; Maricar-Pichon, M.; Rouleau, L.; Bouizi, Y.; Valtchev, V. Core–Shell Zeolite Composite with Enhanced Selectivity for the Separation of Branched Paraffin Isomers. *Microporous Mesoporous Mater.* **2013**, *169*, 212–217.

33. Bouizi, Y.; Majano, G.; Mintova, S.; Valtchev, V. Beads Comprising a Hierarchical Porous Core and a Microporous Shell. *J. Phys. Chem. C* **2007**, *111*, 4535–4542.

34. Lovallo, M. C.; Boudreau, L.; Tsapatsis, M. Preparation of Supported Zeolite Films and Layers: Processing of Zeolite Suspensions and *In Situ* Growth from Homogeneous Solutions. In *Microporous and Macroporous Materials: Symposium Held April 8-11, 1996, San Francisco, California, U.S.A.*; Lobo, R. F., Beck, J. S., Suib, S. L., Corbin, D. R., Davis, M. E., Iton, L. E., Zones, S. I., Eds.; Materials Research Society: Pittsburgh, 1996; Vol. 431, pp 225–236.

35. Okamoto, M.; Osafune, Y. MFI-Type Zeolite with a Core–Shell Structure with Minimal Defects Synthesized by Crystal Overgrowth of Aluminum-Free MFI-Type Zeolite on Aluminum-Containing Zeolite and Its Catalytic Performance. *Microporous Mesoporous Mater.* **2011**, *143*, 413–418.

36. Van Vu, D.; Miyamoto, M.; Nishiyama, N.; Egashira, Y.; Ueyama, K. Selective Formation of *para*-Xylene over H-ZSM-5 Coated with Polycrystalline Silicalite Crystals. *J. Catal.* **2006**, *243*, 389–394.

37. Van Vu, D.; Miyamoto, M.; Nishiyama, N.; Ichikawa, S.; Egashira, Y.; Ueyama, K. Catalytic Activities and Structures of Silicalite-1/H-ZSM-5 Zeolite Composites. *Microporous Mesoporous Mater.* **2008**, *115*, 106–112.

38. Vu, D. V.; Miyamoto, M.; Nishiyama, N.; Egashira, Y.; Ueyama, K. Morphology Control of Silicalite/HZSM-5 Composite Catalysts for the Formation of *para*-Xylene. *Catal. Lett.* **2009**, *127*, 233–238.

39. Lombard, A.; Simon-Masseron, A.; Rouleau, L.; Cabiac, A.; Patarin, J. Synthesis and Characterization of Core/Shell Al-ZSM-5/Silicalite-1 Zeolite Composites Prepared in One Step. *Microporous Mesoporous Mater.* **2010**, *129*, 220–227.

40. Mores, D.; Stavitski, E.; Verkleij, S. P.; Lombard, A.; Cabiac, A.; Rouleau, L.; Patarin, J.; Simon-Masseron, A.; Weckhuysen, B. M. Core–Shell H-ZSM-5/Silicalite-1 Composites: Brønsted Acidity and Catalyst Deactivation at the Individual Particle Level. *Phys. Chem. Chem. Phys.* **2011**, *13*, 15985–15994.

41. Persson, A. E.; Schoeman, B. J.; Sterte, J.; Otterstedt, J. E. Synthesis of Stable Suspensions of Discrete Colloidal Zeolite (Na, TPA)ZSM-5 Crystals. *Zeolites* **1995**, *15*, 611–619.

42. Cundy, C. S.; Cox, P. A. The Hydrothermal Synthesis of Zeolites: Precursors, Intermediates and Reaction Mechanism. *Microporous Mesoporous Mater.* **2005**, *82*, 1–78.

43. Lupulescu, A. I.; Rimer, J. D. *In Situ* Imaging of Silicalite-1 Surface Growth Reveals the Mechanism of Crystallization. *Science* **2014**, *344*, 729–732.

44. Ren, N.; Subotić, B.; Bronić, J.; Tang, Y.; Sikirić, M. D.; Mišić, T.; Svetličić, V.; Bosnar, S.; Jelić, T. A. Unusual Pathway of Crystallization of Zeolite ZSM-5 in a Heterogeneous System: Phenomenology and Starting Considerations. *Chem. Mater.* **2012**, *24*, 1726–1737.

45. Ren, N.; Bosnar, S.; Bronić, J.; Dutour Sikirić, M.; Mišić, T.; Svetličić, V.; Mao, J. J.; Antonić Jelić, T.; Hadžija, M.; Subotić, B. Role of Subcolloidal (Nanosized) Precursor Species in the Early Stage of the Crystallization of Zeolites in Hetero-geneous Systems. *Langmuir* **2014**, *30*, 8570–8579.

46. Davis, T. M.; Drews, T. O.; Ramanan, H.; He, C.; Dong, J.; Schnablegger, H.; Katsoulakis, M. A.; Kokkoli, E.; McCormick, A. V.; Penn, R. L.; *et al.* Mechanistic Principles of Nanoparticle Evolution to Zeolite Crystals. *Nat. Mater.* **2006**, *5*, 400–408.

47. Hasan, F.; Singh, R.; Li, G.; Zhao, D. Y.; Webley, P. A. Direct Synthesis of Hierarchical LTA Zeolite *via* a Low Crystallization and Growth Rate Technique in Presence of Cetyltrimethylammonium Bromide. *J. Colloid Interface Sci.* **2012**, *382*, 1–12.

48. Itani, L.; Liu, Y.; Zhang, W. P.; Bozhilov, K. N.; Delmotte, L.; Valtchev, V. Investigation of the Physicochemical Changes Preceding Zeolite Nucleation in a Sodium-Rich Alumino-silicate Gel. *J. Am. Chem. Soc.* **2009**, *131*, 10127–10139.

49. Maldonado, M.; Oleksiak, M. D.; Chinta, S.; Rimer, J. D. Controlling Crystal Polymorphism in Organic-Free Synthesis of Na-Zeolites. *J. Am. Chem. Soc.* **2013**, *135*, 2641–2652.

50. Althoff, R.; Schulz-Dobrick, B.; Schüth, F.; Unger, K. Con-trolling the Spatial-Distribution of Aluminum in ZSM-5 Crystals. *Microporous Mater.* **1993**, *1*, 207–218.

51. Hughes, A. E.; Wilshier, K. G.; Sexton, B. A.; Smart, P. Aluminum Distribution in ZSM-5 as Determined by X-Ray Photoelectron Spectroscopy. *J. Catal.* **1983**, *80*, 221–227.

52. Kosslick, H.; Fricke, R. Chemical Analysis of Aluminosilicates, Aluminophosphates and Related Molecular Sieves. In *Characterization II*; Karge, H., Weitkamp, J., Eds.; Springer: Berlin, 2007; Vol. 5, pp 1–66.

53. Gorte, R. J. What Do We Know About the Acidity of Solid Acids? *Catal. Lett.* **1999**, *62*, 1–13.

54. Kofke, T. J. G.; Gorte, R. J.; Kokotailo, G. T. Stoichiometric Adsorption Complexes in B-ZSM-5 and Fe-ZSM-5 Zeolites. *J. Catal.* **1989**, *116*, 252–262.

55. Jones, A. J.; Carr, R. T.; Zones, S. I.; Iglesia, E. Acid Strength and Solvation in Catalysis by MFI Zeolites and Effects of the Identity, Concentration and Location of Framework Heteroatoms. *J. Catal.* **2014**, *312*, 58–68.

56. Gounder, R.; Iglesia, E. Catalytic Consequences of Spatial Constraints and Acid Site Location for Monomolecular Alkane Activation on Zeolites. *J. Am. Chem. Soc.* **2009**, *131*, 1958–1971.

57. O'Connor, C. T.; Möller, K. P.; Manstein, H. The Effect of Silanization on the Catalytic and Sorption Properties of Zeolites. *CATTECH* **2001**, *5*, 172–182.

58. Odedairo, T.; Balasamy, R. J.; Al-Khattaf, S. Influence of Mesoporous Materials Containing ZSM-5 on Alkylation and Cracking Reactions. *J. Mol. Catal. A: Chem.* **2011**, *345*, 21–36.

59. Sun, Y. Y.; Han, Y.; Yuan, L.; Ma, S. Q.; Jiang, D. H.; Xiao, F. S. Microporosity in Ordered Mesoporous Aluminosilicates Characterized by Catalytic Probing Reactions. *J. Phys. Chem. B* **2003**, *107*, 1853–1857.

60. Pham, T. N.; Sooknoi, T.; Crossley, S. P.; Resasco, D. E. Ketonization of Carboxylic Acids: Mechanisms, Catalysts,

and Implications for Biomass Conversion. *ACS Catal.* **2013**, *3*, 2456–2473.

61. Corma, A.; Fornes, V.; Forni, L.; Marquez, F.; Martinez-Triguero, J.; Moscotti, D. 2,6-Di-*tert*-Butyl-Pyridine as a Probe Molecule to Measure External Acidity of Zeolites. *J. Catal.* **1998**, *179*, 451–458.

62. Koo, J.-B.; Jiang, N.; Saravanamurugan, S.; Bejblová, M.; Musilová, Z.; Čejka, J.; Park, S.-E. Direct Synthesis of Carbon-Templating Mesoporous ZSM-5 Using Microwave Heating. *J. Catal.* **2010**, *276*, 327–334.

63. Hedlund, J.; Mintova, S.; Sterte, J. Controlling the Preferred Orientation in Silicalite-1 Films Synthesized by Seeding. *Microporous Mesoporous Mater.* **1999**, *28*, 185–194.

64. Li, Q. H.; Wang, Z.; Hedlund, J.; Creaser, D.; Zhang, H.; Zou, X. D.; Bons, A. J. Synthesis and Characterization of Colloidal Zoned MFI Crystals. *Microporous Mesoporous Mater.* **2005**, *78*, 1–10.

65. Li, Y.; Lubchenko, V.; Vekilov, P. G. The Use of Dynamic Light Scattering and Brownian Microscopy to Characterize Protein Aggregation. *Rev. Sci. Instrum.* **2011**, *82*, 053106.

66. Provencher, S. W. CONTIN—A General Purpose Constrained Regularization Program for Inverting Noisy Linear Algebraic and Integral Equations. *Comput. Phys. Commun.* **1982**, *27*, 229–242.

67. Fedeyko, J. M.; Rimer, J. D.; Lobo, R. F.; Vlachos, D. G. Spontaneous Formation of Silica Nanoparticles in Basic Solutions of Small Tetraalkylammonium Cations. *J. Phys. Chem. B* **2004**, *108*, 12271–12275.

68. Rimer, J. D.; Lobo, R. F.; Vlachos, D. G. Physical Basis for the Formation and Stability of Silica Nanoparticles in Basic Solutions of Monovalent Cations. *Langmuir* **2005**, *21*, 8960–8971.

69. de Moor, P.; Beelen, T. P. M.; Komanschek, B. U.; Diat, O.; van Santen, R. A. *In Situ* Investigation of Si-TPA-MFI Crystallization Using (Ultra-) Small- and Wide-Angle X-Ray Scattering. *J. Phys. Chem. B* **1997**, *101*, 11077–11086.

70. Kragten, D. D.; Fedeyko, J. M.; Sawant, K. R.; Rimer, J. D.; Vlachos, D. G.; Lobo, R. F.; Tsapatsis, M. Structure of the Silica Phase Extracted from Silica/(TPA)OH Solutions Containing Nanoparticles. *J. Phys. Chem. B* **2003**, *107*, 10006–10016.

71. Kumar, S.; Wang, Z. P.; Penn, R. L.; Tsapatsis, M. A Structural Resolution Cryo-TEM Study of the Early Stages of MFI Growth. *J. Am. Chem. Soc.* **2008**, *130*, 17284.

72. Schoeman, B. J. Analysis of the Nucleation and Growth of TPA-Silicalite-1 at Elevated Temperatures with the Emphasis on Colloidal Stability. *Microporous Mesoporous Mater.* **1998**, *22*, 9–22.

73. Watson, J. N.; Iton, L. E.; White, J. W. *In Situ* Observation of the Growth of Silicalite Nuclei by Small-Angle X-Ray and Neutron Scattering. *Chem. Commun.* **1996**, 2767–2768.

74. Rimer, J. D.; Fedeyko, J. M.; Vlachos, D. G.; Lobo, R. F. Silica Self-Assembly and the Synthesis of Microporous and Mesoporous Silicates. *Chem.—Eur. J.* **2006**, *12*, 2926–2934.

75. Miyamoto, M.; Kamei, T.; Nishiyama, N.; Egashira, Y.; Ueyama, K. Single Crystals of ZSM-5/Silicalite Composites. *Adv. Mater.* **2005**, *17*, 1985.